Front. Earth Sci. 2022, 16(1): 158–174
https://doi.org/10.1007/s11707-021-0923-8

RESEARCH ARTICLE

The impact of vertical resolution on the simulation of Typhoon Lekima (2019) by a cloud-permitting model

Mengjuan LIU (✉)[1,2], Lin DENG[1,2], Wei HUANG[1,2], Wanchen WU[1,2]

1 Shanghai Typhoon Institute, China Meteorological Administration, Shanghai 200030, China
2 Key Laboratory of Numerical Modeling for Tropical Cyclone of China Meteorological Administration, Shanghai 200030, China

Abstract The impact of vertical resolution on the simulation of Typhoon Lekima (2019) is investigated using the Weather Research and Forecasting (WRF) model version 3.8.1. Results show that decreasing vertical grid spacing from approximately 1000 m to 100 m above 1 km height barely influences the simulated track. However, significant differences are found in the simulated tropical cyclone (TC) structure. The simulation with the coarsest vertical resolution shows a clear double warm-core structure. The upper warm core weakens and even disappears with the increase of vertical resolution. A broader eye and a more slantwise eyewall are observed with the increase of vertical resolution due to the vertically extended lower-level and upper-level outflow, which likely results in a weaker subsidence. Vertical grid convergence is evaluated with the simulated kinetic energy (KE) spectra. As the vertical grid spacing becomes finer than 200 m, convergent KE spectra are found in both the free atmosphere and the outer core of the TC. However, sensitivity tests reveal that the grid convergence is sensitive to the choice of the planetary boundary layer scheme.

Keywords vertical resolution, tropical cyclone, warm core, kinetic energy spectra

1 Introduction

Over the past few decades, horizontal grid spacing in numerical weather prediction (NWP) has decreased by over an order of magnitude from O(100 km) to O(10 km) (Skamarock et al., 2019). In comparison, refinement of the vertical grid is much less. Studies have shown that typical vertical resolution used in NWP models, which is about 0.5 km in the free troposphere, can be insufficient for the accuracy of the model forecasts (Hamilton et al., 1999; Lane et al., 2000).

For quasi-geostrophic (QG) motions away from boundaries, the grid should be consistent with the QG aspect ratio f/N, where f is the Coriolis parameter and N is the buoyancy frequency (Charney, 1949). Therefore, the vertical resolution should be fine enough to resolve horizontal-grid-scale QG vortices (Lindzen and Foxrabinovitz, 1989), i.e., $\Delta z \approx (f/N)\Delta x$, where Δx and Δz are the horizontal and vertical grid spacing, respectively. Finer vertical resolution may be necessary for the presence of fronts. Pecnick and Keyser (1989) related the grid aspect ratio $\Delta z/\Delta x$ to the frontal slope in the idealized two-dimensional frontogenesis simulations by $\Delta z \leqslant m_{\text{slope}}\Delta x$, where m_{slope} is approximately 5×10^{-3} in their simulation. Therefore, for synoptic scale QG motions and fronts, the appropriate grid aspect ratio $\Delta z/\Delta x$ ranges from approximately 0.005 to 0.01.

For the sufficiently small horizontal grid spacing used in mesoscale models, the grid-scale motion is no longer QG. Sub-QG motions include stratified turbulence, gravity waves, and moist convection. Waite (2016) and Cullen (2017) suggested that:

$$\Delta z \leqslant L_{\text{b}} = 2\pi U/N, \tag{1}$$

where L_{b} is the buoyancy scale, and U is the characteristic horizontal velocity scale. Typical atmospheric values for L_{b} range from several hundred meters to 1 km (Waite, 2016).

Watanabe et al. (2015) examined inertia-gravity waves in the stratosphere and suggested that 200–300 m vertical grid spacing is needed to resolve such waves. Skamarock et al. (2019) used the Model of Prediction across Scales (MPAS) to examine the effect of vertical resolution on the convergence of the simulated Kinetic Energy (KE) spectrum and atmospheric flow structures. Both exhibit convergence in the free atmosphere for a 15-km horizontal

Received July 26, 2020; accepted June 21, 2021

E-mail: liumj@typhoon.org.cn

mesh when $\Delta z \leqslant 200$ m. Both studies show the necessity of having vertical grid spacing finer than 200 m when inertia-gravity waves in the stratosphere are taken into consideration. However, there is no consensus for the necessary vertical grid spacing in the simulation of tropical cyclone (TC) yet.

TCs are one of the most destructive natural phenomena in the world (Chen et al., 2019; Yu and Chen, 2019). Although the prediction of TC tracks improved significantly in the past decades, the forecast of TC intensity still remains a challenge (DeMaria et al., 2014). Rogers et al. (2006) suggested inadequate computational resources to run operational models at high horizontal and vertical resolution as one of the factors hindering the improvement of TC intensity forecasts. However, few studies have paid attention to the impact of vertical resolution on TC structure. Bryan and Rotunno (2009) found that convergence in maximum azimuthal velocity is achieved for radial grid spacing of 1 km and vertical grid spacing of 250 m in an axisymmetric numerical model. In terms of full three-dimensional atmospheric model, Zhang and Wang (2003, hereafter ZW03) first investigated the effect of vertical resolution on the simulation of Hurricane Andrew using a mesoscale model with a fine horizontal grid size of 6 km. They found that the increased vertical levels tend to produce a deeper storm with lower central pressure and more precipitation. Kimball and Dougherty (2006, hereafter KD06), investigated the relationship between the storm intensity and the distribution of vertical levels for an idealized hurricane simulation with a fixed number of 24 vertical levels. They found that the distribution of vertical levels in the inflow, outflow, and middle layers of the atmosphere clearly affects the intensity, size, and structure of the storms. Using the Weather Research and Forecasting (WRF) model at horizontal grid size of 10 km, Ma et al. (2012, hereafter M12) found that the simulated TC intensity is weakened when the vertical model levels in the middle troposphere are increased. Zhang et al. (2015, hereafter Z15) further tested the sensitivity of idealized TC under varying background flows and initial vortexes intensities to vertical resolutions in Hurricane Weather Research and Forecasting (HWRF) and revealed that TC intensity with higher vertical resolutions is less sensitive to varying background flows, and stronger TC vortices at the model initial time are less sensitive to the distribution of vertical layers. Zhang et al. (2016) used the operational HWRF model to estimate the effect of model vertical resolution on the track forecasts of TC, where positive impact is found with higher vertical resolution.

Due to the limit of computational resources, the vertical grid sizes in the aforementioned studies are larger than the possible converged vertical grid spacing of 200 m in the free atmosphere, or 250 m in the axisymmetric model. Thanks to the improvement of computing techniques and the expansion of storage, it is possible to carry out simulations with more vertical levels in NWP. This study aims to determine the possible converged vertical grid spacing, as well as the dependence of TC characteristics on vertical grid spacing, by using a near-operational cloud-permitting NWP model.

The rest of the paper is organized as follows. The model setup, experiment design, and a simplified case overview are given in Section 2. In Sections 3.1 and 3.2, the simulated TC structure is investigated. We examine the KE spectra and analyze the possible converged discrete solution in Section 3.3. The results, compared with former studies, are discussed in Section 4. The conclusions follow in Section 5.

2 Experiment design

This study utilizes version 3.8.1 of the WRF model (Skamarock et al., 2008). WRF integrates compressive and non-hydrostatic Euler equations on a terrain-following hydrostatic-pressure vertical η coordinate, defined as

$$\eta = (p - p_t)/(p_s - p_t), \tag{2}$$

where p is the pressure, p_t and p_s are the pressures at the upper and lower boundaries of the model, respectively.

The model domain setup and the physics parameterization suite follow the operational Shanghai Meteorological Service-WRF ADAS Rapid Refresh System (SMB-WARR, Li et al., 2018). The model uses 793 × 853 horizontal grid points with a uniform horizontal spacing of 3 km. The model top is placed at 10 hPa (approximately 31 km above sea level) considering radiance assimilation in the future. Rayleigh damping is applied in the top 7 km. This effective model region is deep enough to allow for overshooting hot towers in the eyewall that can reach heights of up to 18 km as was observed in Hurricane Bonnie (KD06). Key physics parameterizations include the Yonsei University (YSU) scheme (Hong et al., 2006) as the planetary boundary layer (PBL) scheme, the Thompson scheme (Thompson et al., 2004) for microphysics, and the Rapid Radiative Transfer Model for Global climate models (RRTMG) scheme (Iacono et al., 2008) for short- and longwave radiation. Cumulus parameterization is turned off at the 3 km convection-permitting resolution. The initial and lateral boundary conditions are from 6-hourly National Centers for Environmental Prediction Global Forecast System (NCEP GFS) forecasts at 0.5° × 0.5° horizontal resolution. The model is integrated for 72 h from 1200 UTC August 6, 2019 to 1200 UTC August 9, 2019.

To examine potential convergence of vertical resolution and its impact on the simulated TC, four experiments are carried out with varying the number of vertical levels from 40 to 311 levels. Without assigning a specific η level list in WRF, vertical levels below 1 km height are placed with the η values of 1.0, 0.993, 0.983, 0.97, 0.954, 0.934, 0.909, and 0.88. The height of the first model level is 31.5 m. The

levels above approximately 1.5 km are distributed evenly in terms of height. A shallow transition layer lies in between. Four experiments are conducted and named after the number of vertical levels as V40, V70, V161, and V311. Their respective average vertical grid sizes are approximately 1000 m, 500 m, 200 m, and 100 m in the free atmosphere. The four cases span a broad range of vertical spacing, from those commonly used in mesoscale simulations as well as operational NWP, to those meet the requirements of convergence in Section 1. The vertical distributions of grid levels are given in Fig. 1, along with two additional sensitivity tests 46L and 113U to be introduced in Section 4.

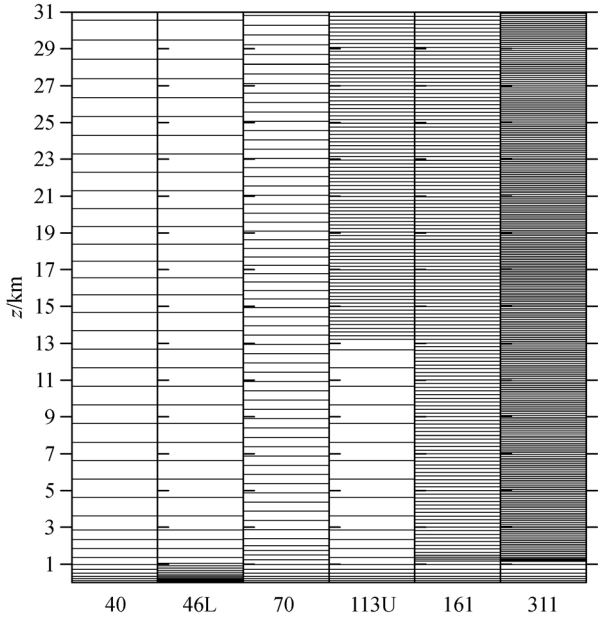

Fig. 1 Vertical distribution of model levels for all experiments.

The selected case TC Lekima (2019) formed to the east of the Philippines on August 4, 2019. It attained its maximum intensity of 915 hPa and stayed as super-typhoon until its landfall. It made landfall in east China with an intensity of 52 $m \cdot s^{-1}$. In terms of precipitation and wind level, Lekima is the strongest and most destructive landfalling TC ever recorded in China. It caused an estimated damage of 40.71 billion yuan, took 45 lives and left three others missing (Zhou et al., 2021).

3 Results

3.1 Track, intensity, and environmental flow

In this subsection, the impact of vertical resolution on TC track, intensity, and environmental flow are discussed. Figure 2 presents the temporal variation of the track, intensity, and vertical wind shear (VWS) of Lekima (2019) in the four simulations. The simulated tracks are mostly consistent with the best track (Lu et al., 2021) estimated by the China Meteorological Administration (CMA). Almost no influence of vertical resolution can be traced until the last 12 h, when the tracks divert into two groups. The two high resolution runs V161 and V311 move less to the west than the low resolution runs V70 and V40. The simulated TC in the V40 experiment moves slightly faster than the other TCs. While the simulated minimum sea level pressure exhibits a consistent temporal trend with the CMA's best track estimate, the magnitudes are under-estimated in all four experiments from simulation hour 6 to 66 as shown in Fig. 2(b). Seeding the simulation with a bogus vortex in the initial field could potentially improve the simulated pressure, but is not attempted in the current study. As this study aims to explore the sensitivity of the simulated TC intensity and structure to vertical resolution rather than the forecast skill of the model, the rest of this section focuses on inter-comparison among sensitivity experiments.

As revealed by the minimum sea level pressure in Fig. 2(b) and maximum azimuthally averaged surface tangential wind speeds in Fig. 2(c), all simulated TCs intensify in the former 42 h. After around 48 h, they reach the minimum central pressure, and then their intensities gradually decrease. The V40 experiment, with the coarsest vertical resolution, produces the most intensive storm with both the lowest central pressure and highest tangential winds. Adding more vertical levels leads to a small yet systematic increase of minimum sea level pressure as shown in Fig. 2(b). However, little differences are found between V161 and V311 in terms of both track and minimum pressure, suggesting convergence beyond 200 m vertical grid spacing.

Figure 2(c) shows the hourly maximum azimuthally averaged tangential wind component at the height of 10 m. All curves are smoothed with a 1-2-1 filter applied 10 times to eliminate noisy signals. Except for the V40 experiment that simulates the largest maximum tangential wind, the differences among the other three experiments are subtle. Stern and Nolan (2012) suggested that minimum central pressure exhibits relatively larger differences among the simulations than that of maximum surface wind, since the maximum wind speed is related to the square root of the pressure anomaly. Besides, the central pressure is more sensitive to the upper structure of the eye, which will be discussed in the next subsection, while the surface winds tend to be affected more by the small-scale convections near the eye-wall as well as the asymmetry of the vortex.

Numerous studies have identified weak vertical wind shear (VWS) that are positively correlated with rapid intensification (RI, an increase of maximum sustained surface winds of at least 30 kt or 15 $m \cdot s^{-1}$ within 24 h (Kaplan et al., 2010)). Figure 2(b) show that in contrast to the best track, no simulated vortexes reach the extent of RI in 36 h. To investigate the discrepancy, the VWS between

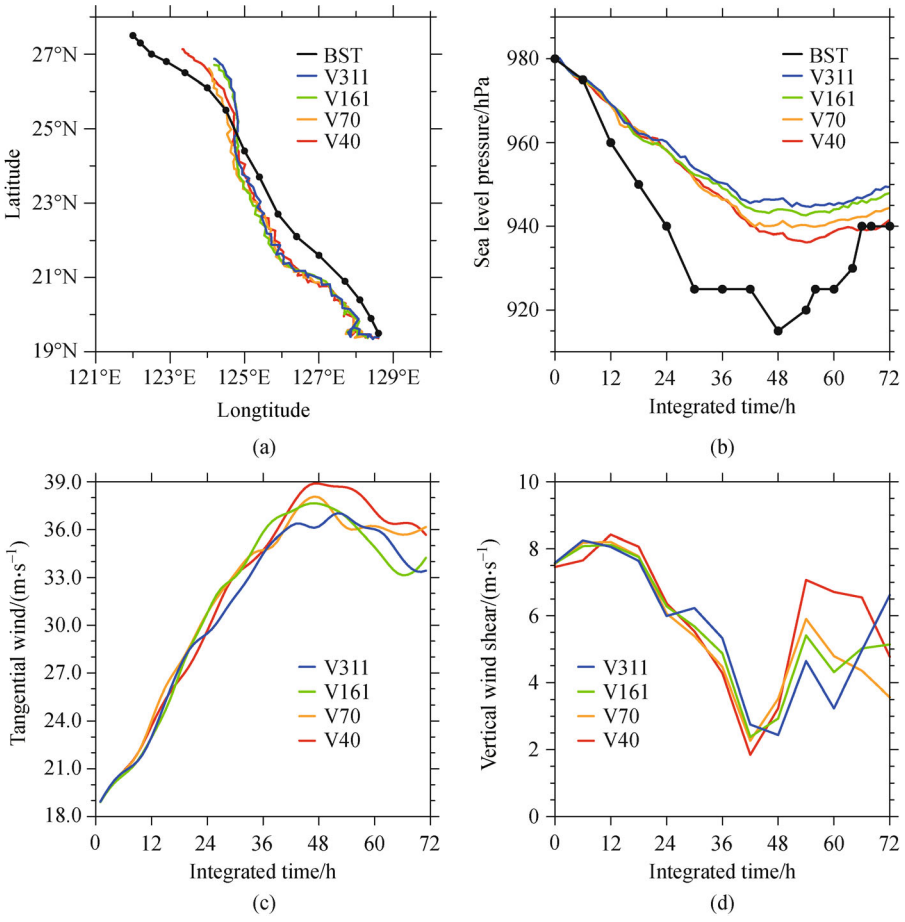

Fig. 2 (a) Tracks, (b) minimum sea level pressure, (c) maximum azimuthally averaged tangential wind at 10 m, and (d) 200–850 hPa shear of horizontal wind ($m \cdot s^{-1}$) for V40, V70, V161, and V311. Black lines in (a) and (b) indicate the best track data provided by CMA.

200 hPa and 850 hPa and within the 200–500 km annulus is presented in Fig. 2(d). The VWS in all four experiments is around 8 $m \cdot s^{-1}$ at the beginning, and then decreases to around 5 $m \cdot s^{-1}$ until 36 h. As climatological studies suggest, the average VWS for TCs that undergo RI is approximately 4–5 $m \cdot s^{-1}$ (Kaplan et al., 2010; Rozoff et al., 2015), the simulated VWS implies an unfavorable condition for RI.

The unfavorable environmental flow is also reflected in Fig. 3, which presents the streamlines at 16 km height, where the peak of the outflow appears at around 36 h. A large area of low-speed (not shown) anticyclonic circulation develops to the north of the vortex in all experiments except V40. The northwestward wind from the outflow encounters the southward environmental wind and forms a front-like pattern, which is denoted by the red line. The area of the broad anticyclonic circulation pushes the front southward with the increase of the vertical levels. In V311, the southern boundary of the circulation bulges to the west of the TC. The westward wind from the outflow bends due to the block of the environment, thus, a trough-like pattern appears denoted by the blue line in Fig. 3(d). The front-like and trough-like patterns between the environment flow and the TC coincides with the relative humidity at the same level. The clear northern and northwestern edges of the shading of the relative humidity in V311 manifest the block of environment. A similar phenomenon was observed by Ryglicki et al. (2019).

3.2 TC structure

Although only minor effects can be seen from the simulated tracks and intensities, varying vertical resolution causes changes to the structure of the TC vortex. One of the most important features of TC is the characteristic warm core, whereby temperature in the center of the TC is higher than its environment (Stern and Nolan, 2012; Stern and Zhang, 2013). Here we define “the environment” to be the (time evolving) mean temperature averaged in the 480–510 km annulus, as 510 km (170 grid points) is the largest radius to ensure the complete moving circle around the TC center falls in the domain during the entire simulation. Figure 4 presents the time-height Hovmöller diagrams of the perturbation temperature in the eye (within 30 km radius from the TC center). Results of two additional tests (V46L and V113U) are also shown here, which will be

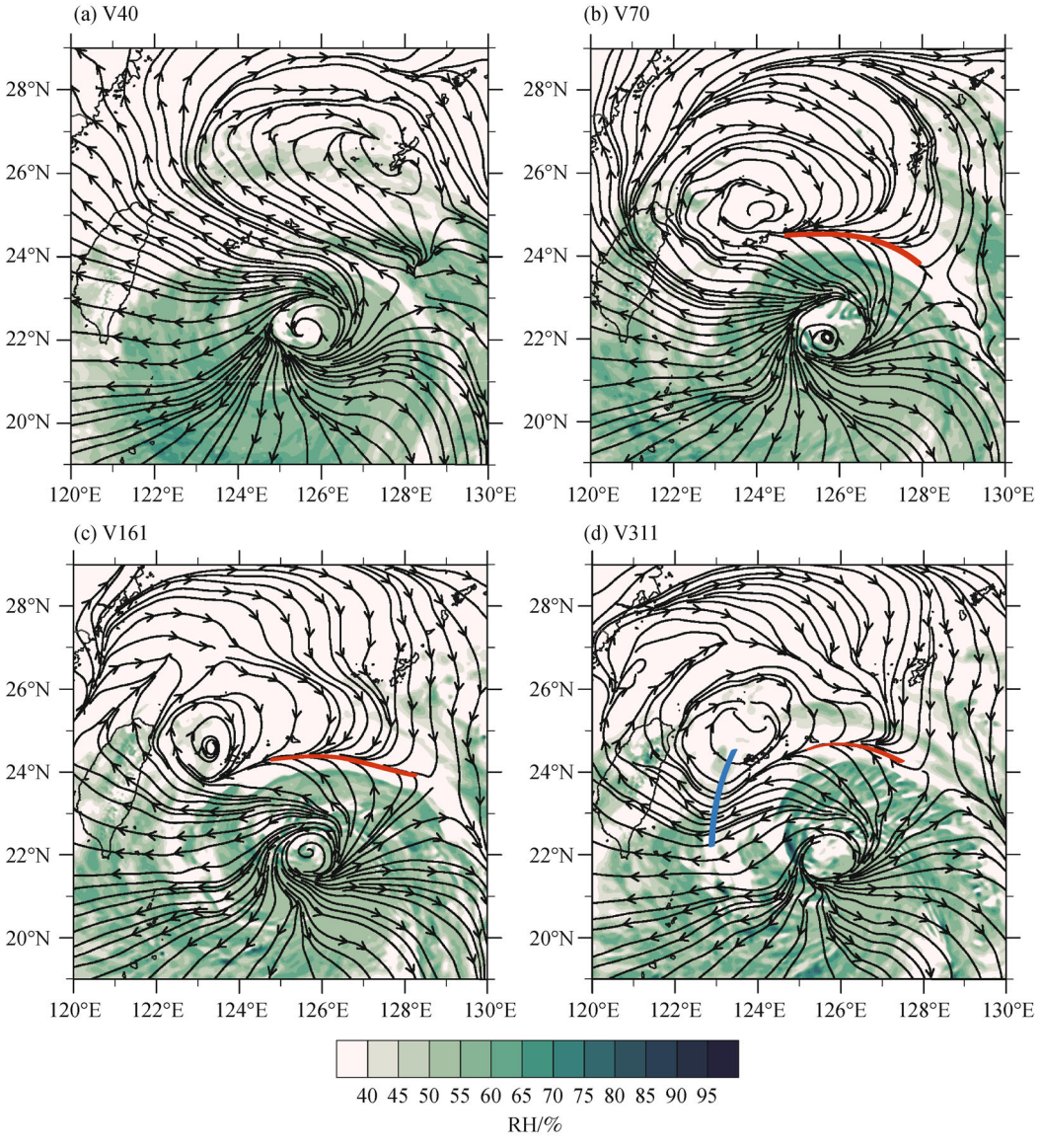

Fig. 3 Snapshots of the instantaneous streamlines and horizontal distribution of the relative humidity (color shading) at 36 h and 16 km height for (a) V40, (b) V70, (c) V161, and (d) V311. The front-like and trough-like patterns are denoted by red and blue lines, respectively.

discussed in Section 4. The evolution of the warm-core structure shows that both V40 and V70 produce a double warm-core structure. The lower core forms between 6 to 10 km above sea level, whereas the upper core is found between 14 to 16 km height. The other experiments only generate the lower warm core, which appears at around 36 h, and persists to the end of the simulation. In V40 (Fig. 4(a)), the upper warm core appears at around 48 h, shortly after the formation of the lower one. The upper warm core in V70 forms at around 54 h (Fig. 4(b)). By comparing the area of + 6 K contour, it can be found that the upper warming weakens significantly with the increase of the vertical levels. The weaker warming agrees with the higher central pressure at sea surface, as shown in Fig. 2(b).

Previous studies demonstrated that the warm core is formed mainly by subsidence in the eye (Zhang et al., 2002; Wang et al., 2019). Weaker subsidence with the increase of the vertical levels is observed in the left panel of Fig. 5. The left panel of Fig. 5 presents the radial-height cross-sections of the equivalent potential temperature θ_e at 60 h, when all simulated storms have reached their mature stage. Since θ_e above the boundary layer is nearly conserved following an air parcel, these contours reflect the flow of air in the storm (Houze, 2010). In the center of the storm above 6 km, θ_e increases significantly with height, as an evidence of subsidence concentrated in the eye of the storm. Figure 5(a) shows relatively dense isopleth of θ_e above 8 km in the simulated eye of V40 compared to the other simulations. The density of

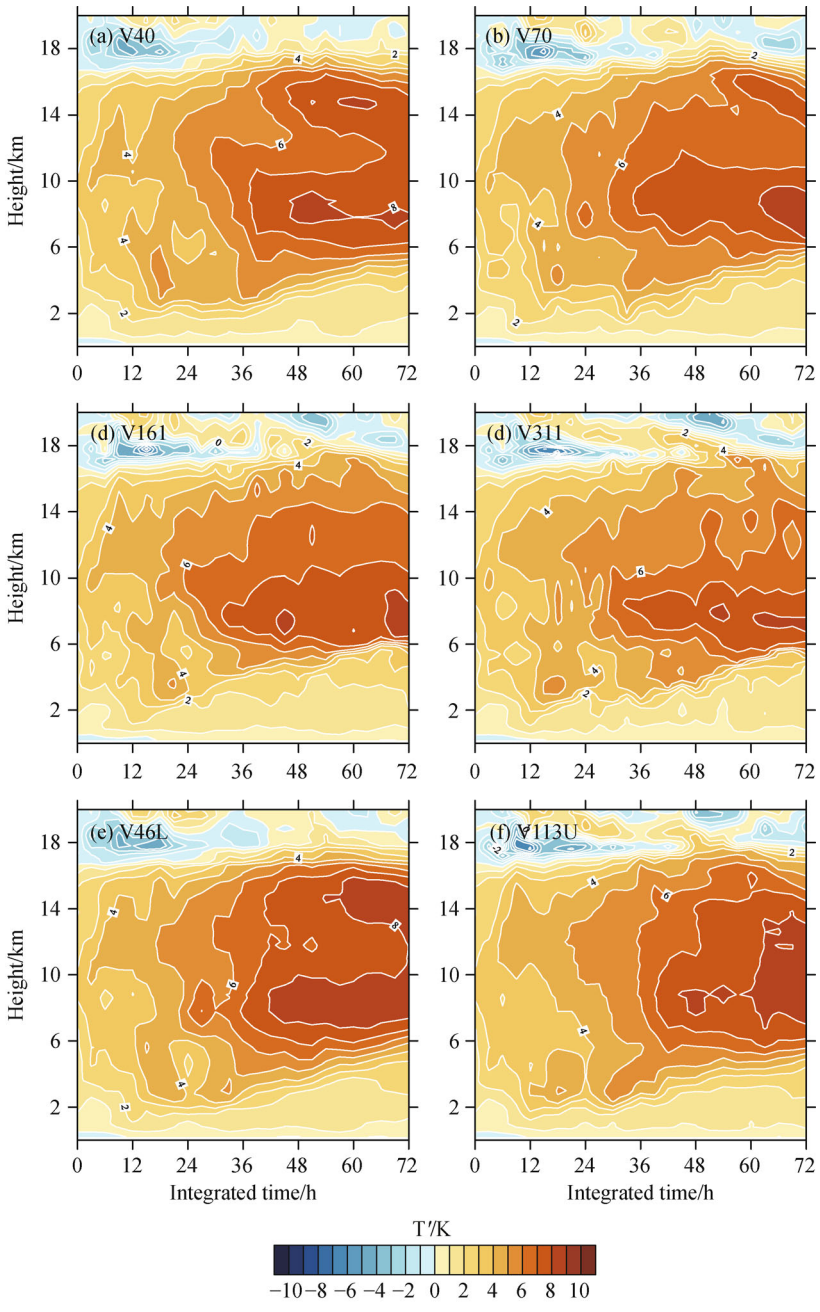

Fig. 4 Time-height Hovmöller diagrams of the perturbation temperature in the eye region (r = 0–30 km) for (a) V40, (b) V70, (c) V161, (d) V311, (e) V46L, and (f) V113U. Data are plotted every 3 h.

contours, as well as θ_e itself in the upper atmosphere decreases with the increase of the vertical levels.

The weaker subsidence with more vertical levels is likely associated with a broader eye and a more slantwise eyewall, as shown in the left panel of Fig. 5. The simulated eyewall begins to slope above the boundary layer. Smith et al. (2008) found that the frictionally enhanced radial inflow in the boundary layer becomes super-gradient in the vicinity of the eyewall and turns radially outward in a layer atop the inflow layer as it seeks gradient balance. This low-level radial flow reversal, in other words, the lower-level outflow, allows air to flow out of the eye region into the base of the eyewall cloud. As shown in Fig. 5(b), a thin layer from 1.5 km to 2 km, which corresponds to the weak and shallow lower-level outflow simulated by V40, carries high-θ_e air from the eye and penetrates into the base of the eyewall. The entrainment of high-θ_e air tends to create conditional instability and intensify vertical motions in the eyewall cloud. However, when more vertical levels are added, the low-level outflow grows stronger and deepens vertically (Figs. 5(d), 5(f), and 5(h)). The deeper outward flow with high-θ_e air pushes the lower part of the eyewall

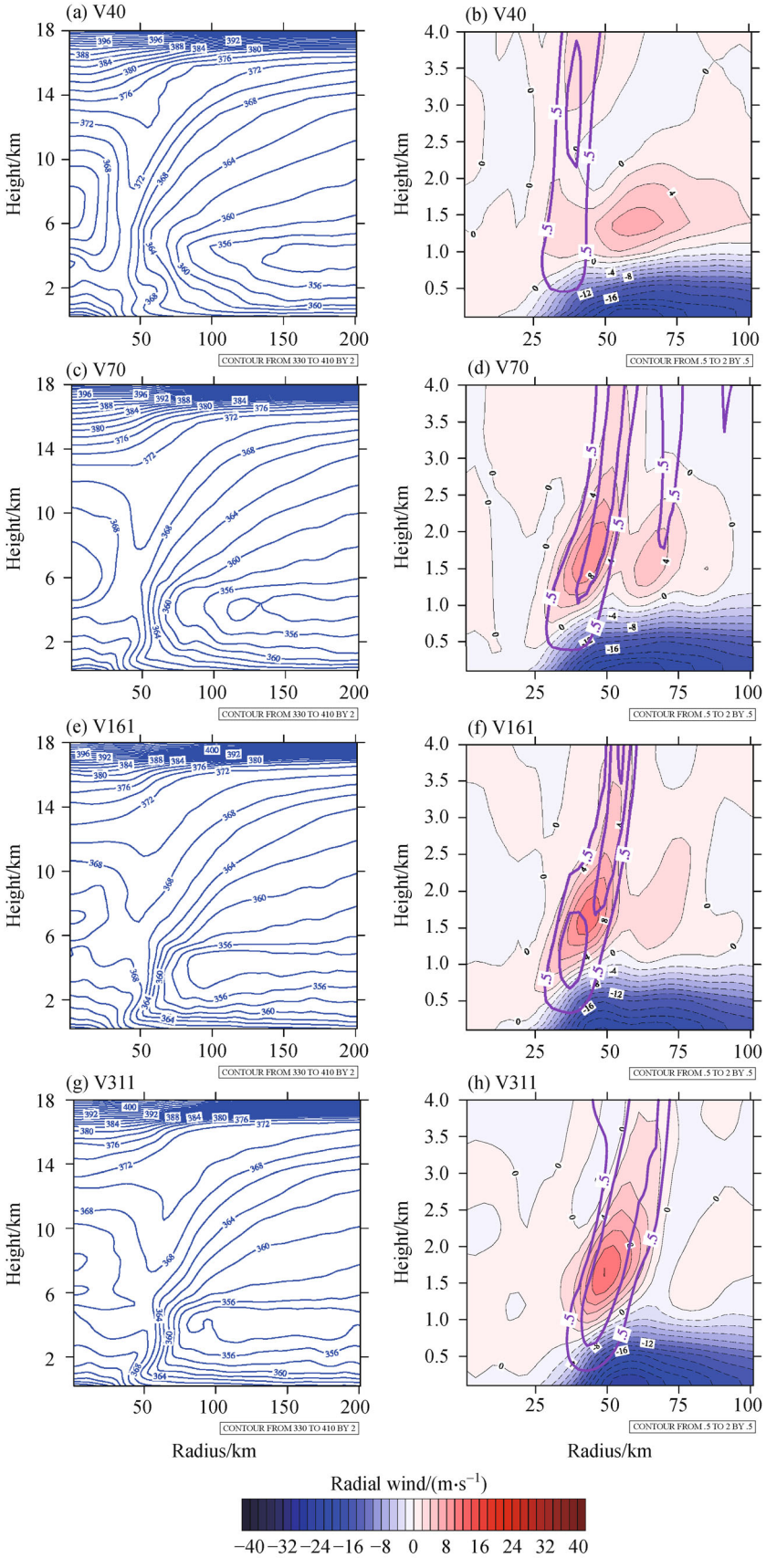

Fig. 5 Radial-height cross sections of the azimuthally averaged equivalent potential temperature on the left panel, and radial wind (color shading) and upward motion (contours) on the right panel at 60 h of the simulation. Contours only include vertical velocity greater than 0.5 $m \cdot s^{-1}$.

outward as manifested by the "nose-like" isopleth in the left panel and by the location of updrafts in the right panel of Fig. 5. With the similar radius of maximum wind (RMW) in the boundary layer, but the farther updrafts from the center, the eyewall is distorted vertically when more vertical levels are added. Similarly, the upper outflow with more vertical levels extends downward near the eyewall as shown in the left panel of Fig. 6, corresponding to a more slantwise eyewall in the upper troposphere.

From the aspect of microphysics, diabatic heating comprises both releasing latent heat through condensation and absorbing latent heat through evaporation. The positive diabatic heating near the storm center is correlated with the eyewall clouds. The right panel of Fig. 6 presents the radial-height cross-section of the azimuthally averaged diabatic heating rates at 36 h, when the warm cores are still developing and the differences among each case are insignificant. Figures 6(b) and 6(h) demonstrate that the eye wall cloud already flares more outward at that moment with the increase of the vertical levels especially below 4 km and above 12 km, where the upper- and lower- outflow extend. It is worth noting that the "secondary eye wall-like" upward motions in Figs. 6(c) and 6(g) are due to the asymmetry of the storm as no closed circulation of the second eye wall or another maximum in surface tangential winds is observed. Since diabatic heating dominates the temperature tendency among all physical parameterizations in our experiments above the inflow layer (figure not shown), the simulated eyewalls are mainly heated by diabatic heating in the clouds. Due to the thermal-wind balance, location of the maximum tangential wind denoted by the orange dash lines in the right panel of Fig. 6 also tilt outward with the increase of the vertical levels. Although adding more vertical levels produces stronger secondary circulation in terms of stronger upward motion and outflow (see left panel of Fig. 6), the broader eye region and more slantwise eyewall may still lead to weaker concentrated subsidence. Besides, Houze (2010) indicated that unlike the upward vertical velocities in the eyewall, the downdrafts in TC show no sloping coherent structure. Downdrafts driven by precipitation in the experiments with more vertical levels tend to go through the cooler and dryer environment rather than the warm and moist eyewall as the eyewall slopes more. Evaporation of rain drops cools the air in the inner-core region, represented by the blue shaded area in the right panel of Fig. 6, hence possibly reduce the radially inward advection of heat.

Another possible factor decreasing the upper warming with more vertical levels could be the height of the cloud top along with the radiative forcing there. As more levels are added in the upper atmosphere, the cloud top of the overriding cirrus canopy can be simulated more precisely. M12 pointed out that the differences in cloud top heights among the experiments with different vertical grid spacing in the upper layer could reach up to several kilometers. Since the magnitude of the outgoing longwave radiation at the top of the atmosphere (hereafter abbreviated as OLR) is correlated with the cloud top height, Fig. 7 suggests that the simulated storm in V40 exhibits the broadest area of high clouds. Although OLR lower than 80 $W \cdot m^{-2}$ is found in the other three experiments, which is probably due to the stronger convection developed in outer rainbands, the area of the closed 90 $W \cdot m^{-2}$ OLR contours decreases with the increase of the vertical levels. Not only the northern and western regions shrink as being affected by the blocking environment flow, but the rest of the anvil clouds in the storm also shrinks. The larger and higher cloud top may help to preserve more heat in the storm from the upward long wave radiation, thus reducing the upper cooling aloft.

3.3 Spectral analysis

Figure 8 presents the compensated KE spectra ($KE \times k^{5/3}$) as a function of the longitudinal wavenumber k at $z = 5$ km, 16 km, and 24 km. These three heights represent the lower troposphere, upper troposphere and lower-middle stratosphere respectively. z = 16 km is also approximately the height of the outflow layer of TC Lekima in its mature stage. These spectra are computed using a one-dimensional spectra decomposition of the velocities (u, v, w) along east–west horizontal grid lines spanning the whole domain, as there is little difference between the spectra computed using lines in the east–west direction, the north–south direction, or an averaged of the two directions (Skamarock, 2004). The energy densities are also time averaged over 48 h simulation time, at 1 h intervals. The energy densities acquired in the east–west direction are averaged over the south-north extent of the domain. The outmost 15 grid points from each lateral boundary are not used to minimize boundary effects.

The spectra in Fig. 8 appear to converge when the vertical grid spacing is less than or equal to 200 m, as V161 and V311 ($\Delta z \approx 200$ m, 100 m) are nearly identical at three heights, while V40 and V70 exhibit lower KE levels in the mesoscale region. In the outflow layer, the time rate of change of total resolved KE is dominated by the shear production term $-\tau_{ij}\frac{\partial \overline{u_i}}{\partial x_j}$ which is proportional to the vertical gradient of the horizontal winds along the height. As Δz reduces, the shear production increases and the total resolved KE tends to grow faster (results not shown). This behavior is consistent with the results of Skamarock et al. (2019).

The KE spectra in cylindrical coordinates are also examined to analyze the impact on the TC. The simulated TC is mapped from a Cartesian coordinate system onto a cylindrical coordinate with its origin located at the vortex center. The data are then interpolated onto annuli at 1° spacing in the azimuthal direction. For each annulus, a one-dimensional array with 360 points is then obtained. The KE spectra are computed based on the detrended array. Radii larger than 60 grid points (180 km) are computed

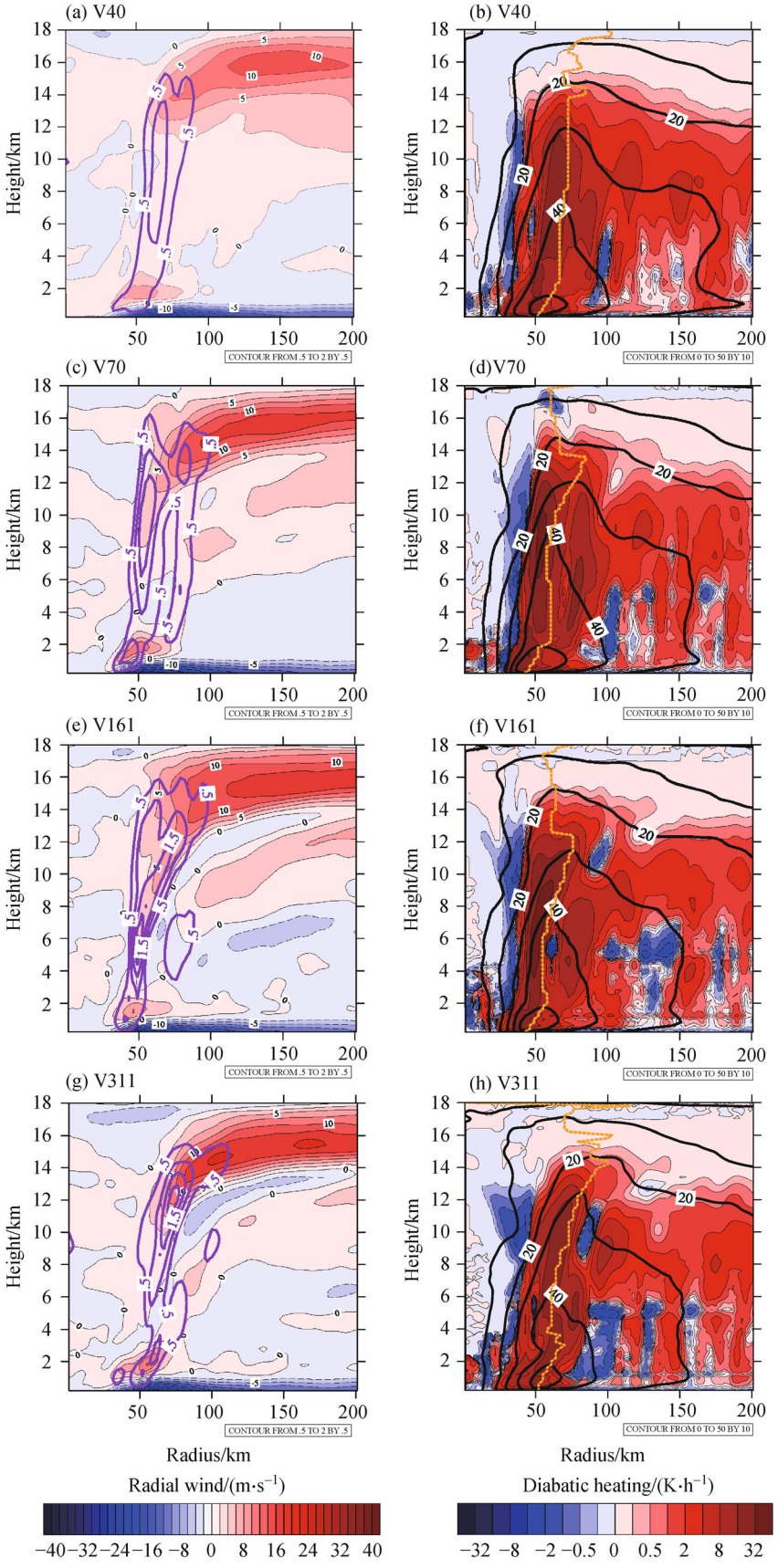

Fig. 6 Left panel (a, c, e, g): radial-height cross sections of the azimuthally averaged radial wind (color shading) and upward motion (contours, vertical velocity greater than 0.5 $m \cdot s^{-1}$); right panel (b, d, f, h): diabatic heating rates (color shading) and tangential winds (contours) at 36 h for all experiments.

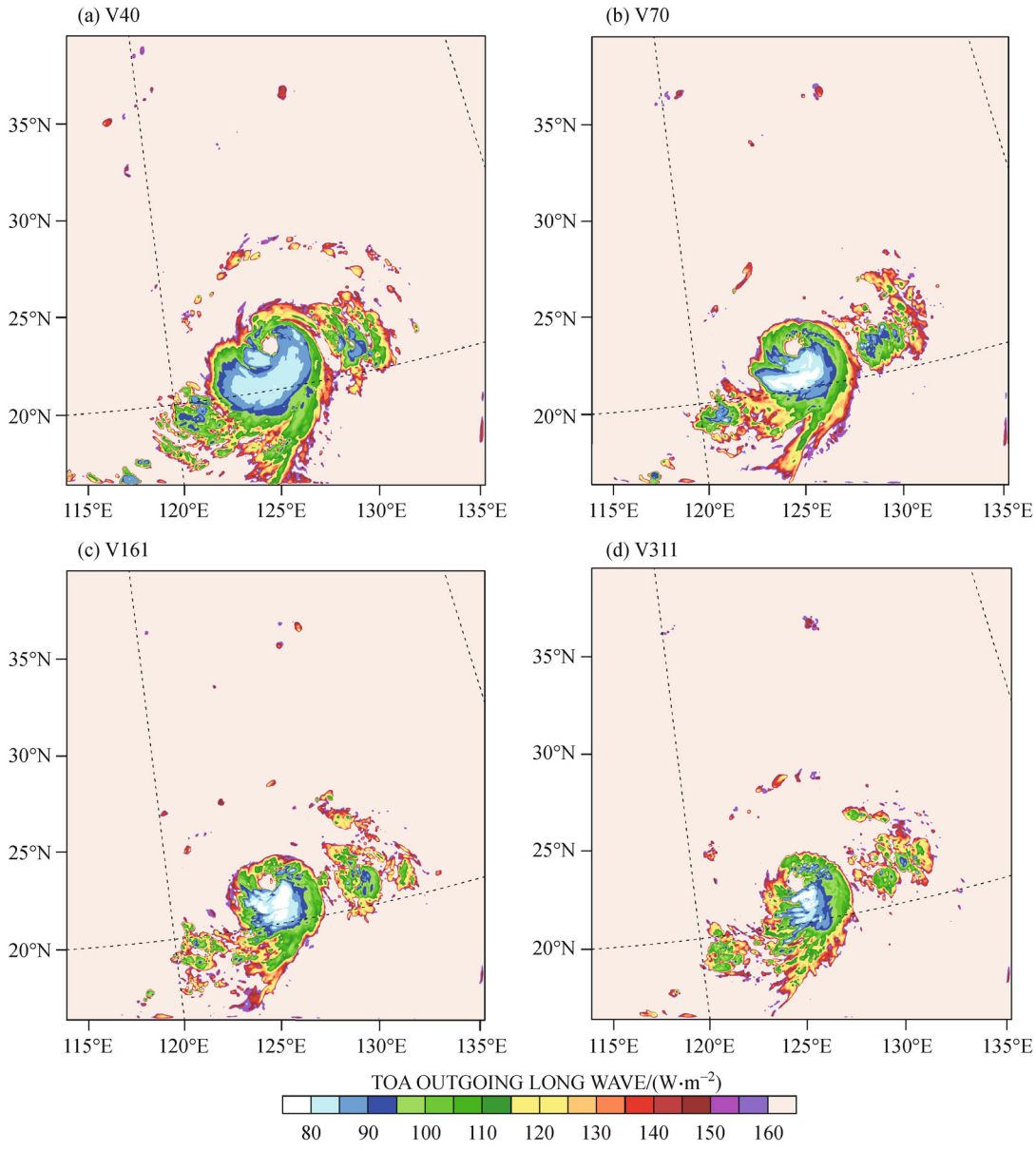

Fig. 7 Outgoing longwave radiation at the top of the atmosphere at 36 h for (a) V40, (b) V70, (c) V161, and (d) V311.

such that enough information along each annulus is guaranteed. Figure 9 presents the azimuthal KE spectra as a function of k at z = 5 km and 16 km. The energy densities are averaged over the radius from 180 km to 200 km, at approximately 4 to 4.5 RMW. The energy densities are also time-averaged from 24 to 72 h simulation, at 1 h intervals. The spectra computed in the cylindrical coordinate show a similar trend as in the Cartesian coordinate, such that the energy densities grow with the increase of the vertical levels at all wavenumbers but are quickly converged when the vertical grid spacing falls below 200 m. The influence on KE spectra is consistent with the former observation that stronger outflow occurs with more vertical levels (Figs. 6(b), 6(d), 6(f), 6(h)).

In the analysis above, when the vertical grid spacing is less than or equal to 200 m, the KE spectra in the free atmosphere exhibit convergence. However, this conclusion is limited to the model configuration we use here. In the experiments conducted by Skamarock et al. (2019), the same PBL scheme was selected as our configuration, though a different model system (MPAS) was used. Since the PBL scheme is one of the dominant sources of vertical filtering, the convergence scale may vary with different PBL schemes.

When a PBL scheme is turned on in WRF, it not only deals with the vertical diffusion within the boundary layer, but also throughout the free atmosphere. This is especially true for convection permitting models. Zhu et al. (2019)

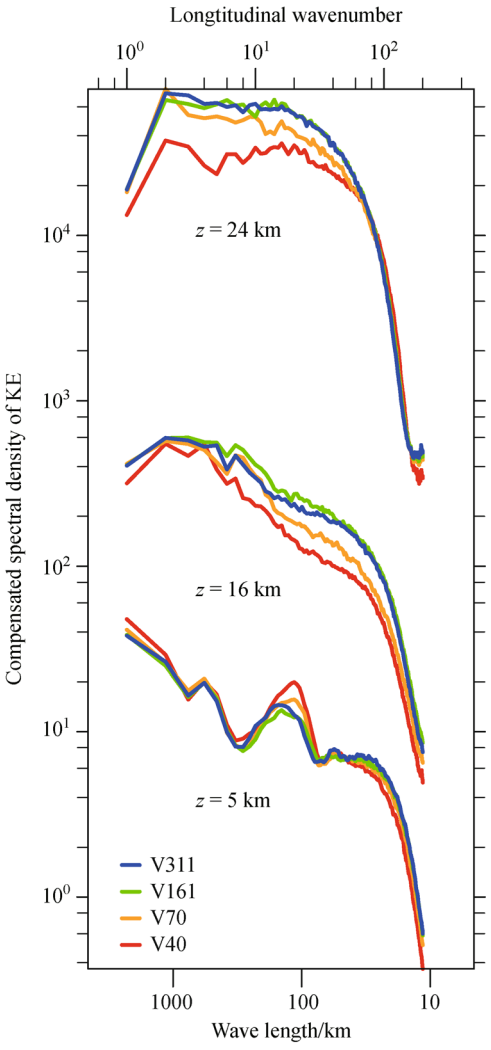

Fig. 8 Compensated horizontal KE (KE × $k^{5/3}$) spectra at z = 5 km, 16 km, and 24 km. For clarity, the z = 16 km and z = 24 km spectra are shifted two and four decades up, respectively.

demonstrated that the intense turbulent mixing generated by cloud processes also exists above the PBL in the eyewall and rainbands of a TC. In the outflow, the parameterization in the free atmosphere determines the vertical diffusion. Vertical eddy diffusivity K^v is shown to have large impacts on the simulation of TCs (Gopalakrishnan et al., 2013). The local K^v in the free atmosphere is greatly affected by vertical grid spacing Δz. Different PBL schemes use different expressions to describe the relationship between Δz and K^v. The YSU scheme in WRF V3.8.1 employs a gradient Richardson number (Rig) based formulation to compute the K^v in the free atmosphere. The diffusivity applied to heat is given by

$$K_H^v = l^2 f(\mathrm{Rig})\left(\frac{\partial U}{\partial z}\right), \tag{3}$$

where l is the mixing length, $f(\mathrm{Rig})$ is a stability function, and $\frac{\partial U}{\partial z}$ is the vertical wind shear. According to Hong et al. (2006) l is parameterized by

$$\frac{1}{l} = \frac{1}{kz} + \frac{1}{\lambda_0}, \tag{4}$$

where a asymptotic length scale $\lambda_0 = 150$ m is adopted, but in the actual implementation in WRF V3.8.1

$$\lambda_0 = \max(\Delta z/10, 30\ \mathrm{m}). \tag{5}$$

The restriction is imposed on λ_0 to avoid too small l with small Δz . This kind of mixing length parameterization was verified by Zhang and Drennan (2012) against *in situ* aircraft data that were collected during four intense hurricanes.

According to our experimental configuration, the length scale l in the free atmosphere are approximately 100 m, 50 m, 30 m, and 30 m for V40, V70, V161, V311, respectively. By comparing the magnitude and amplitude of l^2, $f(\mathrm{Rig})$, and $\left(\frac{\partial U}{\partial z}\right)$, it is found that l^2 is the dominant term in the formulation of K_H^v (figures not shown). Therefore, K_H^v is sensitive to vertical resolution before Δz decreases to 300 m. When $\Delta z \leqslant 300$ m, l does not change anymore due to Eq. (5), and so does K_H^v.

However, formulations of K_H^v are different with other PBL schemes. The Mellor-Yamada-Janjic (MYJ) scheme (Mellor and Yamada, 1982; Janić, 2001) is taken as an example here. K_H^v in the MYJ is determined by

$$K_H^v = lqS_H, \tag{6}$$

where the turbulent kinetic energy (TKE) is denoted by $q^2/2$, S_H is a stability correction factor. Above the PBL, the mixing length l is computed as a fraction of the model grid distance Δz, i.e., $l = 0.23\Delta z$. Therefore, K_H in MYJ is mainly affected by l, which is proportional to Δz. However, unlike the YSU scheme, the MYJ imposes no limits on l, which means that K_H can alter significantly even when Δz varies from 200 m to 100 m.

To examine the impact of different PBL schemes, four sensitivity experiments are carried out with the same vertical resolutions and configurations except that the MYJ scheme is used for PBL parameterization. Figures 10 and 11 present the KE spectra of the MYJ experiments at z = 16 km in both Cartesian and cylindrical coordinates. Difference can be found even between V161 and V311, which implies that the convergence of KE has not yet been reached at 200 m when the MYJ scheme is used.

4 Discussion

The observation from the previous section that more vertical levels above 1 km are correlated with the slightly weaker vortex seems to contradict some of the results from

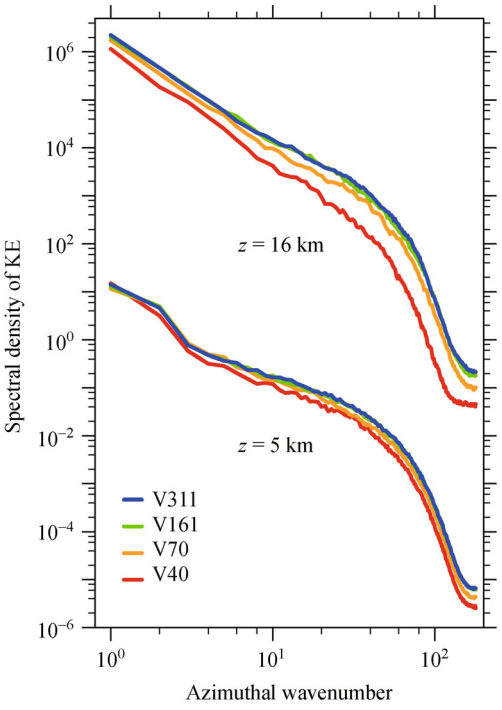

Fig. 9 Azimuthal KE spectra at z = 5 and 16 km for V40, V70, V161, and V311. For clarity, the z = 16 km spectra are shifted six decades up.

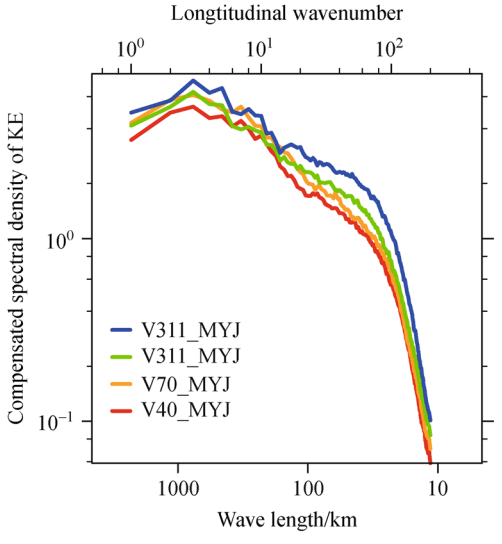

Fig. 10 Compensated horizontal KE (KE × $k^{5/3}$) spectra at z = 16 km for V40_MYJ, V70_MYJ, V161_MYJ, and V311_MYJ.

previous studies mentioned in Section 1, for example, ZW03 found that increasing vertical resolution tends to produce a deeper storm. In this section, some possible explanations are given by comparing this study with them. Table 1 gives a brief summary of the experimental design of ZW03, KD06, M12, Z15, and this study.

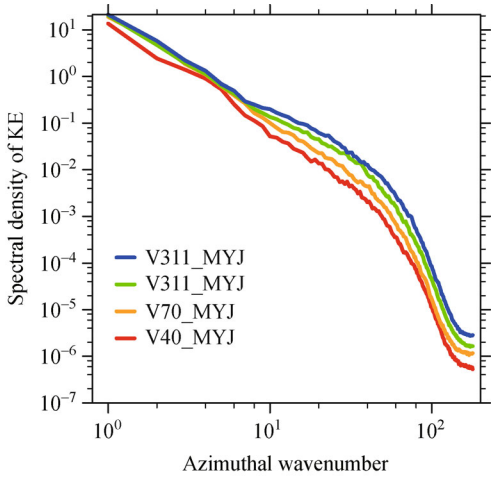

Fig. 11 Azimuthal KE spectra at z = 16 km for V40_MYJ, V70_MYJ, V161_MYJ, and V311_MYJ.

Firstly, ZW03, M12, and this study are real-case studies focusing on different storms (Table 1). KD06 pointed out that in real cases, features of the environmental flow may develop differently in simulations with different vertical resolutions. This will lead to complex feedback processes that would be difficult to isolate from the influences of vertical resolution alone. As it has been investigated in Section 3, the upper environmental flow is indeed influenced by vertical resolution, and inhibits the intensification of the storm. The environmental characteristics may lead to different influences on the simulated TC and its sensitivity to vertical resolution. Secondly, different suites of the model physics are used in these studies, for example, some turn on the cumulus scheme while the others don't. Different physical parameterization may yield different dependence on vertical resolution. Pope et al. (2001) demonstrated that complex interactions between different parameterizations in convectively active areas can also lead to sensitivities with respect to vertical levels.

Last but not the least, previous studies examined the sensitivity through varying the location of η levels given a relatively small number of vertical levels. This is because these studies were restricted to looking for optimal solutions with limited numbers of vertical levels, due to computational resource limits at that time. This is also reflected by the lower model top height set between 100 and 50 hPa (Table 1), which is around 16 km to 21 km. The largest number of vertical levels they used were 35, 61, 64, and 69, which means that the averaged Δz in their studies was no more than 300 m. Z15 also found that increasing vertical resolution from 21 to 43 levels produced stronger TCs, whereas increasing it further to 64 levels did not intensify the TC further. Note that by using uniform or stretched Δp, the smallest Δz only appears at the bottom of the model, leaving the upper level with rather large Δz. Lindzen and Foxrabinovitz (1989) proposed the danger of

Table 1 Summary of key model parameters

Study	Case	Model	Model domain and grid spacing		
			Δx/km	P_{top}/hPa	nz
ZW03	Hurricane Andrew (1992)	MM5	54, 18, 6	50	23, 32, 35, 46, 69
KD06	idealized	MM5	15, 5	100	24, 35
M12	Typhoon Talim (2005)	WRF 3.2	30, 10	50	34, 36, 53, 61
Z15	idealized	HWRF	27, 9, 3	50	21, 32, 43, 64
This study	Typhoon Lekima (2019)	WRF 3.8.1	3	10	40, 70, 161, 311

models whose vertical structure was described in terms of approximately uniform Δp, since at upper levels these models would have large Δz and therefore larger $\Delta z/\Delta x$. The danger exists with stretching Δp too, especially when the critical outflow layer lies mostly above 10 km height.

With the development of computer techniques and the expanding storage, it is possible to test evenly distributed levels in height with higher model top in atmospheric models today. The finest resolution in this study, approximately 100 m, is beyond the possible convergence Δz from previous studies (e.g., Skamarock et al., 2019). The positive correlation between the storm intensity and vertical levels is not guaranteed among all Δz. Bryan and Rotunno (2009) also found an increase in the intensity as Δz increases from 250 m to 1000 m. Additionally, as the model top reaches 10 hPa, the stratosphere can be properly resolved providing a more flexible upper boundary than the lower model top as mentioned in KD06. The impact of a more flexible upper boundary has not yet been investigated either.

We find similarities with prior studies when drawing our attention from the final "product" of the TC simulation, such as intensity, back to the intermediate processes. For example, all these studies suggest that more intense secondary circulation is correlated with more vertical levels in critical layers. To test if other conclusions in former studies apply to constant height intervals in this study, two more experiments (V46L and V113U) are conducted.

4.1 Adding more levels below 1 km

Since the majority of this article discusses the influence of varying vertical levels above 1 km, this work would be incomplete without investigating the dependence of vertical levels below 1 km. Moreover, the boundary layer processes are crucial for TC modeling as the storm inflow depends strongly on model levels in the PBL. Therefore, the V46L experiment is conducted by adding 6 extra levels below 1 km, as shown in Fig. 1. The 13th level is slightly raised from the height of the 7th level in V40 to ensure a gradual increase of Δz with height. The first level is fixed to isolate the influence from surface fluxes, since previous model simulations (KD06, M12) have confirmed that the TC intensity and structure are sensitive to the height of surface layer (Ma et al., 2014).

Figure 12 shows the temporal variation of TC intensity for V46L (orange) in comparison with V40 (red). The minimum sea level pressure starts to decrease at 24 h when more vertical layers are added. The difference of central pressure between case V40 and V46L grows with time till 48 h and is maintained at about 5 hPa afterwards. The variation of the azimuthal tangential wind is consistent with the central pressure. Figure 4(e) shows that the eye in

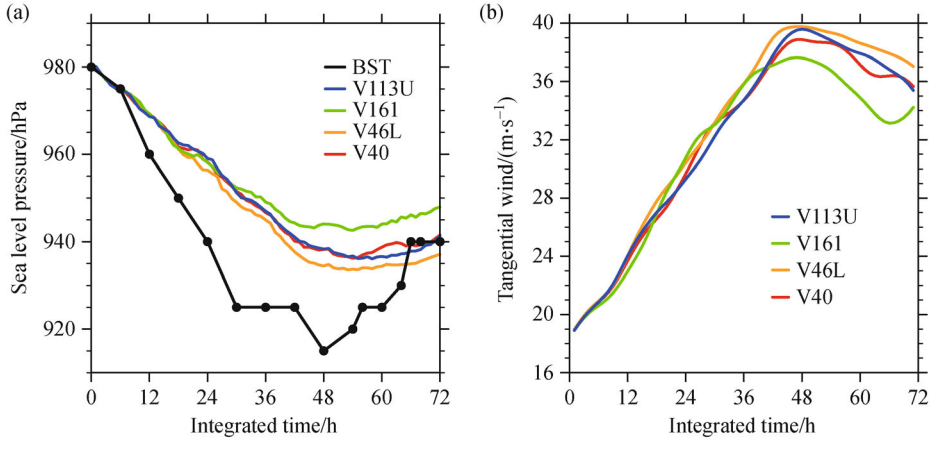

Fig. 12 (a) Minimum sea level pressure and (b) maximum azimuthally averaged tangential wind at 10 m height for V46L and V113U in comparison with V40 and V161.

V46L is warmer from 8 km to 16 km height with the same double warm-core structure as in V40, which demonstrates again the importance of the inflow layer through transporting heat from the sea surface to the storm. The conclusion that the increase of the vertical resolution in the boundary layer results in a more intensive TC is consistent with the previous studies (ZD03, M12, Z15).

4.2 Reducing levels in the middle layer

ZW03, KD06, M12, and Z15 all evaluated the impact of the upper layer or outflow layer by manually splitting the vertical levels at η = 0.11, 0.44, 0.25, and 0.3, respectively. By separately investigating the influence of different layers, M12 found that increasing the vertical levels in the middle atmosphere inhibits the TC intensification, while increasing vertical levels in the upper layer produces a slightly stronger TC. ZW03 speculated that changing the upper-level vertical resolution does not have significant impacts. KD06 argued that adding a few levels to an already adequately resolved outflow layer did not lead to a large impact in storm intensity. In their tests, increasing only the upper-level vertical resolution of the 23-level case to a total of 35 levels produced a weaker storm. Z15 also found that increasing the upper-layer vertical resolution generates weaker storms.

As the height of the outflow layer differs in different tropical cyclones, evolves with time, and is sensitive to vertical resolution, it is hard to determine a universal outflow layer height for all TCs at all times. For an operational model, a TC is only one of the synoptic systems that occurs in the domain, occupying a rather limited area (i.e. in this case roughly 1.5% of the model domain). However, to test the findings from the above-mentioned studies, a simple experiment named V113U is designed by combining η levels under 13 km in V40 and the η levels above 13 km in V161, as shown in Fig. 1. This case offers an interesting comparison by both reducing the number of vertical grids in the middle layer of V161 and adding layers in the upper atmosphere of V40. The height of 13 km is determined after observing the evolution of the outflow layer in the experiments in Section 3. Figure 12 shows the temporal variation of the TC intensity in terms of the central pressure and the surface wind speeds. The intensity of V113U is almost identical to V40 and becomes stronger than V161 after 42 h. V113U has only one warm core (Fig. 4(f)), which is formed at roughly the same level as V161, but extends to 14 km at 60 h. The storm center above 10 km height from 48 h to the end of the simulation in V113U is warmer than that in V161 by more than 1 K, which suggests stronger warming in the eye with fewer levels in the middle layer. Figure 13 gives the radial-height cross section of both the equivalent potential temperature below 18 km and the secondary circulation below 4 km. As the levels in the middle layer are kept the same as V40, the lower outflow only exists in the same thin layer as in V40, while the upper outflow stretches deeper into the eyewall than V40 (not shown). An almost vertically erect eyewall develops in accordance with stronger upper warming in the eye than V161. Above 14 km, as more vertical levels are added, the influence of cloud radiation is reflected in the weaker warming compared to V40 (Figs. 4(a) and 4(f)).

M12 elucidated that increasing the mid-level resolution may lead to enhanced vertical gradient of the vertical velocity, which could cause stronger convergence of cold and dry environmental air. Figure 14 presents the evolution of the relative humidity at 9 km in the outer region of the TC for V40, V113U, and V161. When the upper levels are

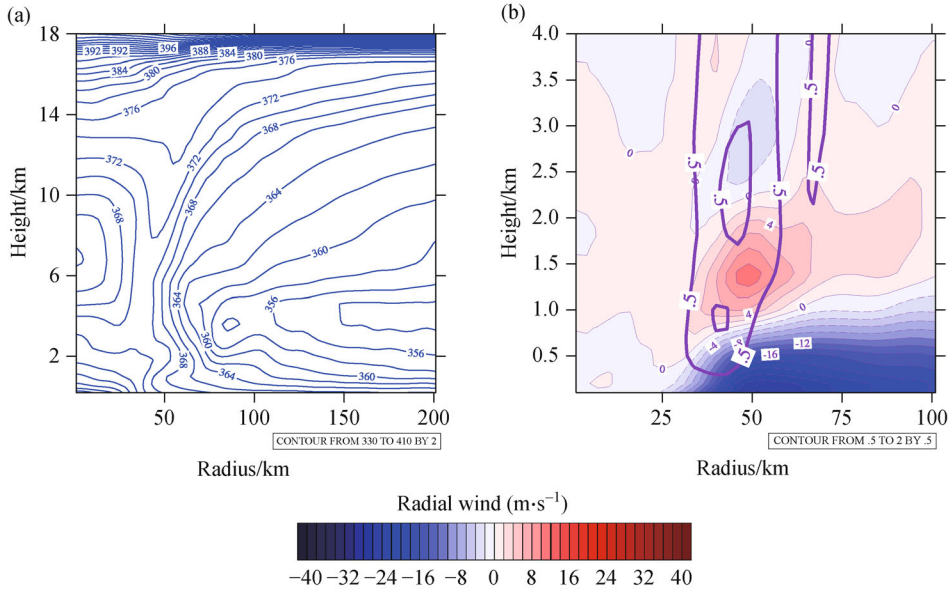

Fig. 13 As in Fig. 5 but for V113U.

kept the same, adding more levels in the middle layer (from V113U to V161) results in a reduced relative humidity by 6%. Increasing the upper level resolution from V40 to V113U leads to only minor decreases in the relative humidity. The convergence forces cold and dry environmental air into the TC inner core, thus inhibiting the eye from warming up. The slight decrease in intensity with the increase of the upper level resolution also agrees with ZW03, KD06, and Z15. The comparison reveals similar results as the previous studies when the experiments are designed in a similar manner.

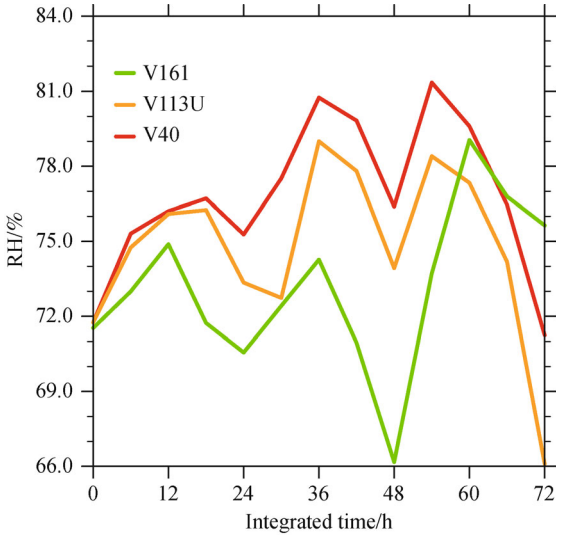

Fig. 14 Time series of the average relative humidity (%) in the outer region of the TC at 9 km for V40, V113U and V161. The values are averaged within the annulus of 150–300 km from the TC center.

5 Summary and concluding remarks

This study investigates the sensitivity of a simulated TC to the vertical grid spacing ranging from approximately 1000 m to 100 m in the free atmosphere. Four 72-h experiments are conducted using a near-operational configuration of WRF with 3 km horizontal grid size. Detailed analyses of the sensitivity tests show that.

1) Varying vertical resolution barely influences the TC track in this study. In terms of TC intensity, the increase of vertical levels leads to higher central pressure to a small degree. The surface wind shows less sensitivity to vertical resolution, since the central pressure is more sensitive to the upper warming in the eye.

2) Varying vertical resolution influences the environmental flow around the TC. At 16 km height, a large area of anti-cyclonic circulation develops to the north of the TC in all experiments except V40, and forms a front-like structure, which inhibits TC intensification.

3) Varying vertical resolution influences the structure of the TC. V40 and V70 both simulate double warm-core structures with one core located between 6 – 10 km and the other in the 14 – 16 km layer. The other two experiments with smaller Δz simulate only a single warm core between 6 – 10 km. The upper warming weakens with the increase of vertical levels. There are two possible factors for the decrease of the upper level warming.

a) Weaker subsidence in the eye. Although the increase of vertical levels leads to a stronger secondary circulation, the lower-level and upper-level outflows extend vertically to form a broader eye and a more slantwise eyewall, which may lead to weaker subsidence in the eye. Additionally, the more slantwise convection leads to more hydrometeors falling into the cooler and dryer environment, which likely increases evaporation and reduces the radially inward advection of heat.

b) The experiment with more vertical levels, especially in the upper atmosphere, can simulate a finer cloud-top structure than the experiment with coarser vertical grid spacing, and therefore has a lower cloud top above most parts of the storm. Note that a higher cloud top may help to preserve more heat in the storm from less upward long wave radiation.

4) When the vertical grid spacing is less than or equal to 200 m, the KE spectra in the free atmosphere and in the outer-core of the simulated TC exhibit convergence. However, the converged grid spacing may change with different PBL schemes, if they use different parameterizations for eddy diffusivity, as the vertical eddy diffusivity in the free atmosphere is considerably affected by vertical grid spacing.

In contrast to the prior studies, it is found that adding more vertical levels slightly decreases the intensity of the simulated TC. The difference in conclusions may be explained with the use of evenly distributed levels in height, much finer vertical resolution, more elevated model top, an unfavorable environment which is sensitive to the vertical resolution, and a different suite of physical parameterization. Therefore, some of the conclusions may be restrict to the specific case here. Our findings suggest that the stronger secondary circulation is not necessarily correlated to a stronger storm. To further investigate the relationship between very high vertical resolution and the structure of TC, an idealized simulation with the capacity of detailed budget analysis is needed.

Together with former studies, it can be seen that the best simulation of TC track and intensity is not necessarily produced by the finest vertical resolution. The non-monotonicity exposes the limitation of NWP that benefits to forecasts with improved resolution is not guaranteed. The discussion also implies that the specific choices of physics parameterization can affect the sensitivity of vertical resolution. The cloud top is determined by the hydrometeors parameterized by microphysics schemes, and its radiative effect through radiation schemes. PBL schemes play an important role in the inflow layer (Nolan

et al., 2009a, 2009b) and are not confined within the PBL (Zhu et al., 2019). Model physics adds uncertainty to the relationship between the simulated TC and vertical resolution. From the aspect of operational models, this study implies that it is not necessary to increase the vertical resolution at the moment. More effort could be put on improving the performance of physics schemes under sufficiently fine vertical resolution.

Finally, although abundant computational resources today offer an opportunity to simulate TC at very high horizontal resolution, such as numerous large-eddy simulations of both idealized and real TCs with $\Delta z \leqslant$ 100 m (Zhu, 2008; Rotunno et al., 2009; Green and Zhang, 2015; Ito et al., 2017; Wang and Jiang, 2017; Wu et al., 2019), the distribution of vertical levels is similar to that adopted in current mesoscale models: most of which have less than 100 levels overall, with refined grid spacing in the boundary layer and incrementally stretched spacing in the free atmosphere. Therefore, analysis of model results especially for the fine structures in the free atmosphere, must be carried out with caution as the vertical resolution may not have reached convergence according to this study.

Acknowledgements We thank Dr. Jianwen Bao from NOAA/ESRL/PSD for his support and helpful discussions. We thank the anonymous reviewers for their constructive comments. We thank Prof. Bowen Zhou from Nanjing University, Dr. Martin Köhler from Deutscher Wetterdienst and Dr. Shiwei Sun from Nanjing Joint Institute for Atmospheric Sciences for their reviews. This study was sponsored by the Research Program from Science and Technology Committee of Shanghai (No.19dz1200101), the National Key Research and Development Program of China (No. 2016YFE0109700) and the National Natural Science Foundation of China (Grant No. 42075012).

References

Bryan G H, Rotunno R (2009). The maximum intensity of tropical cyclones in axisymmetric numerical model simulations. Mon Weather Rev, 137(6): 1770–1789

Charney J G (1949). On a physical basis for numerical prediction of large-scale motions in the atmosphere. J Meteorol, 6(6): 371–385

Chen P, Yu H, Xu M, Lei X, Zeng F (2019). A simplified index to assess the combined impact of tropical cyclone precipitation and wind on China. Front Earth Sci, 13(4): 672–681

Cullen M J P (2017). The impact of high vertical resolution in the Met Office Unified Model. Q J R Meteorol Soc, 143(702): 278–287

DeMaria M, Sampson C R, Knaff J A, Musgrave K D (2014). Is tropical cyclone intensity guidance improving? Bull Am Meteorol Soc, 95(3): 387–398

Gopalakrishnan S G, Marks F Jr, Zhang J A, Zhang X, Bao J W, Tallapragada V (2013). A study of the impacts of vertical diffusion on the structure and intensity of the tropical cyclones using the high-resolution HWRF system. J Atmos Sci, 70(2): 524–541

Green B W, Zhang F (2015). Numerical simulations of Hurricane Katrina (2005) in the turbulent gray zone. J Adv Model Earth Syst, 7(1): 142–161

Hamilton K, Wilson R J, Hemler R S (1999). Middle atmosphere simulated with high vertical and horizontal resolution versions of a GCM: improvements in the cold pole bias and generation of a QBO-like oscillation in the tropics. J Atmos Sci, 56(22): 3829–3846

Hong S Y, Noh Y, Dudhia J (2006). A new vertical diffusion package with an explicit treatment of entrainment processes. Mon Weather Rev, 134(9): 2318–2341

Houze R A Jr (2010). Clouds in tropical cyclones. Mon Weather Rev, 138(2): 293–344

Iacono M J, Delamere J S, Mlawer E J, Shephard M W, Clough S A, Collins W D (2008). Radiative forcing by long-lived greenhouse gases: calculations with the AER radiative transfer models. J Geophys Res D Atmospheres, 113(D13): D13103

Ito J, Oizumi T, Niino H (2017). Near-surface coherent structures explored by large eddy simulation of entire tropical cyclones. Sci Rep, 7(1): 3798

Janić Z I (2001). Nonsingular implementation of the Mellor-Yamada level 2.5 scheme in the NCEP Meso model

Kaplan J, DeMaria M, Knaff J A (2010). A revised tropical cyclone rapid intensification index for the Atlantic and eastern North Pacific Basins. Weather Forecast, 25(1): 220–241

Kimball S K, Dougherty F C (2006). The sensitivity of idealized hurricane structure and development to the distribution of vertical levels in MM5. Mon Weather Rev, 134(7): 1987–2008

Lane D E, Somerville R C J, Iacobellis S F (2000). Sensitivity of cloud and radiation parameterizations to changes in vertical resolution. J Clim, 13(5): 915–922

Li J, Chen B, Huang W, Zhang X (2018). Investigation of the impact of cloud initialization on numerical prediction of a convective system. J Trop Meteorol, 34: 198–208

Lindzen R S, Foxrabinovitz M (1989). Consistent vertical and horizontal resolution. Mon Weather Rev, 117(11): 2575–2583

Lu X, Yu H, Ying M, Zhao B, Zhang S, Lin L, Bai L, Wan R (2021). Western North Pacific Tropical Cyclone Database created by the China Meteorological Administration. Adv Atmos Sci, 38: 690– 699

Ma Z, Fei J, Huang X, Cheng X (2012). Sensitivity of tropical cyclone intensity and structure to vertical resolution in WRF. Asia-Pac J Atmospheric Sci, 48(1): 67–81

Ma Z, Fei J, Huang X, Cheng X (2014). Impacts of the lowest model level height on tropical cyclone intensity and structure. Adv Atmos Sci, 31(2): 421–434

Mellor G L, Yamada T (1982). Development of a turbulence closure-model for geophysical fluid problems. Rev Geophys, 20(4): 851–875

Nolan D S, Stern D P, Zhang J A (2009a). Evaluation of planetary boundary layer parameterizations in tropical cyclones by comparison of *in situ* observations and high-resolution simulations of Hurricane Isabel (2003). Part II: inner-core boundary layer and eyewall structure. Mon Weather Rev, 137(11): 3675–3698

Nolan D S, Zhang J A, Stern D P (2009b). Evaluation of planetary boundary layer parameterizations in Tropical Cyclones by comparison of *in situ* observations and high-resolution simulations of Hurricane Isabel (2003). Part I: initialization, maximum winds, and the outer-core boundary layer. Mon Weather Rev, 137(11): 3651–3674

Pecnick M J, Keyser D (1989). The effect of spatial-resolution on the simulation of upper-tropospheric frontogenesis using a sigma-

coordinate primitive equation model. Meteorol Atmos Phys, 40(4): 137–149

Pope V D, Pamment J A, Jackson D R, Slingo A (2001). The representation of water vapor and its dependence on vertical resolution in the Hadley Centre Climate Model. J Clim, 14(14): 3065–3085

Rogers R, Aberson S, Black M, Black P, Cione J, Dodge P, Dunion J, Gamache J, Kaplan J, Powell M, Shay N, Surgi N, Uhlhorn E (2006). The intensity forecasting experiment: a NOAA multiyear field program for improving Tropical Cyclone intensity forecasts. Bull Am Meteorol Soc, 87(11): 1523–1538

Rotunno R, Chen Y, Wang W, Davis C, Dudhia J, Holland G J (2009). Large-eddy simulation of an idealized Tropical Cyclone. Bull Am Meteorol Soc, 90(12): 1783–1788

Rozoff C M, Velden C S, Kaplan J, Kossin J P, Wimmers A J (2015). Improvements in the probabilistic prediction of tropical cyclone rapid intensification with passive microwave observations. Wea. Forecasting, 30, 1016–1038

Ryglicki D R, Doyle J D, Hodyss D, Cossuth J H, Jin Y, Viner K C, Schmidt J M (2019). The unexpected rapid intensification of Tropical Cyclones in moderate vertical wind shear. Part III: outflow-environment interaction. Mon Weather Rev, 147(8): 2919–2940

Skamarock W C (2004). Evaluating mesoscale NWP models using kinetic energy spectra. Mon Weather Rev, 132(12): 3019–3032

Skamarock W C, Klemp J, Dudhia J, Gill D O, Barker D, Wang W, Powers J G (2008). A Description of the Advanced Research WRF Version 3. NCAR Tech Note, NCAR/TN-475 + STR, 1–113

Skamarock W C, Snyder C, Klemp J B, Park S (2019). Vertical resolution requirements in atmospheric simulation. Mon Weather Rev, 147(7): 2641–2656

Smith R K, Vogl S, (2008). A simple model of the hurricane boundary layer revisited. Quarterly Journal of the Royal Meteorological Society, 134, 337–351

Stern D P, Nolan D S (2012). On the height of the warm core in tropical cyclones. J Atmos Sci, 69(5): 1657–1680

Stern D P, Zhang F (2013). How does the eye warm? Part I: a potential temperature budget analysis of an idealized Tropical Cyclone. J Atmos Sci, 70(1): 73–90

Thompson G, Rasmussen R M, Manning K (2004). Explicit forecasts of winter precipitation using an improved bulk microphysics scheme. Part I: description and sensitivity analysis. Mon Weather Rev, 132(2): 519–542

Waite M L (2016). Dependence of model energy spectra on vertical resolution. Mon Weather Rev, 144(4): 1407–1421

Wang H, Wang Y, Xu J, Duan Y (2019). Evolution of the warm-core structure during the eyewall replacement cycle in a numerically simulated Tropical Cyclone. J Atmos Sci, 76(8): 2559–2573

Wang S, Jiang Q (2017). Impact of vertical wind shear on roll structure in idealized hurricane boundary layers. Atmos Chem Phys, 17(5): 3507–3524

Watanabe S, Sato K, Kawatani Y, Takahashi M (2015). Vertical resolution dependence of gravity wave momentum flux simulated by an atmospheric general circulation model. Geosci Model Dev, 8(6): 1637–1644

Wu L, Liu Q, Li Y (2019). Tornado-scale vortices in the tropical cyclone boundary layer: numerical simulation with the WRF–LES framework. Atmos Chem Phys, 19(4): 2477–2487

Yu H, Chen L (2019). Impact assessment of landfalling tropical cyclones: introduction to the special issue. Front Earth Sci, 13(4): 669–671

Zhang B, Lindzen R S, Tallapragada V, Weng F, Liu Q, Sippel J A, Ma Z, Bender M A (2016). Increasing vertical resolution in US models to improve track forecasts of Hurricane Joaquin with HWRF as an example. Proc Natl Acad Sci USA, 113(42): 11765–11769

Zhang D, Liu Y, Yau M (2002). A multiscale numerical study of Hurricane Andrew (1992). Part V: inner-core thermodynamics. Mon Weather Rev, 130(11): 2745–2763

Zhang D, Wang X (2003). Dependence of hurricane intensity and structures on vertical resolution and time-step size. Adv Atmos Sci, 20(5): 711–725

Zhang D, Zhu L, Zhang X, Tallapragada V (2015). Sensitivity of idealized hurricane intensity and structures under varying background flows and initial vortex intensities to different vertical resolutions in HWRF. Mon Weather Rev, 143(3): 914–932

Zhang J A, Drennan W M (2012). An observational study of vertical eddy diffusivity in the hurricane boundary layer. J Atmos Sci, 69(11): 3223–3236

Zhu P (2008). Simulation and parameterization of the turbulent transport in the hurricane boundary layer by large eddies. J Geophys Res, 113: D17104

Zhu P, Tyner B, Zhang J A, Aligo E, Gopalakrishnan S, Marks F D, Mehra A, Tallapragada V (2019). Role of eyewall and rainband eddy forcing in tropical cyclone intensification. Atmos Chem Phys, 19 (22): 14289–14310

Zhou C, Chen P, Yang S, Zheng F, Yu H, Tang J, Lu Y, Chen G, Lu X, Zhang X, Sun J (2021). The impact of Typhoon Lekima (2019) on East China: a postevent survey in Wenzhou city and Taizhou city. Front Earth Sci